

## **Bio-inspired Patterned Surface for Submicron Particle Deposition in a Fully Developed Turbulent Duct**

### **ABSTRACT**

Arrays of surface ribs have been reported to significantly enhance particle collection efficiency in particle removal devices. However, the surface ribs also cause a higher pressure drop. Therefore, the overall performance needs to take into consideration the above factors. In this study, different forms of surface ribs inspired by nature were designed and parametric studies were performed to enhance deposition efficiency. Our parametric studies comprised three different aspects; geometry of the patterned surface, pitch-to-height ratio, and particle size. The flow field around patterned surfaces was simulated in a two-dimensional channel flow by using the Reynolds stress model, corrected by turbulence velocity fluctuation in the wall-normal direction. The particle trajectory was solved by using Lagrangian particle tracking. When the overall efficiency ratio was considered, a semi-circular pattern had the best overall efficiency with 1137 times increase when compared to the case without patterns. Although the open-circular pattern has the minimum particle deposition enhancement, the overall efficiency of the open-circular pattern has 862 times increase compared to the case without patterns. Surface ribs (semi-circular, triangular and rectangular) can achieve a higher particle deposition velocity, but a higher flow resistance is generated compared with applying the open-circular surface ribs. The deposition location was then investigated for different surface ribs at different pitch-to-height ratios ( $p/e$ ). This study shows that the semi-circular surface pattern should be recommended to enhance the overall performance of particle removal devices,

especially for submicron particles.

**Keywords: Bio-inspired, Surface Rib Array, Particle Deposition, Submicron Particles, Fully**

## **Developed Turbulent Flow**

### **Nomenclature**

$A$	cross-section area of the duct
$C_c$	Cunningham correlation
$C_D$	particle drag coefficient
$C_\mu$	empirical constant specified in the turbulent model
$d$	particle size
$D_h$	hydraulic diameter
$f$	friction factor
$F$	component of particle forces
$h$	channel height
$J$	particle flux
$k$	turbulence kinetic energy
$N_d$	number of deposited particles
$N_0$	initial particle numbers
$n_0$	particle number per volume
$p$	pressure
$pe$	duct perimeter
$Re$	Reynolds number
$S$	particle to air density ratio
$t$	deposition duration
$u$	air velocity
$u^*$	friction velocity
$u_d$	particle deposition velocity
$u_p$	local velocity of particle
$U_{mean}$	mean velocity
$U_{free}$	freestream velocity
$y$	vertical position of the channel
$\alpha$	contact angle
$\eta$	efficiency index
$\nu$	kinematic viscosity of air
$\mu$	dynamic viscosity of air
$\rho$	density of air
$\tau$	particle relaxation time
$\tau_w$	wall shear stress

### **Subscripts**

$i, j$	vector and/or tensor indices
$+$	nondimensionalization

$g$  gas phase  
 $p$  particle phase

## 1. INTRODUCTION

The number concentration of **particulate matters** (PM) significantly affects indoor air quality. The demands to deposit PM, especially in the range of 0.1 to 1  $\mu\text{m}$  are intense, however, the restraints come from the low efficiency of submicron particle deposition in many air cleaners and energy-inefficiency with the aerodynamics of air cleaners currently used. The removal of submicron PMs is difficult due to their tiny size. This is the most challenging size range to be filtered because neither interception, inertial impaction, nor the Brownian diffusion mechanism dominates. A higher collection efficiency of submicron particles can be achieved by electric filters which are composed of permanently charged electric fibers, but the efficiency decreases exponentially with the operation time due to particle loading (Ji et al. 2003). This low energy-efficient device not only increases costs but also accelerates the exhaustion of limited electricity that is available. Suh and Kim (1996) indicated that particle deposition could be enhanced by using a surface treatment method in a “two-stage electrostatic precipitator”. It arouses the interest of studying the surface treatment by using various shapes of micro-structured surfaces could be a potential method to enhance the effectiveness of existing air cleaners. Lu and Lu (2015) studied the effects of surface rib shapes (rectangular riblet surface, triangular ribbed-wall and full-circular ribbed-wall) on particle deposition in turbulent duct flows. They defined an efficiency ratio by considering both effects of particle deposition enhancement and drag force induced by a micro-structured surface. The full-circular ribbed-wall surface suffered the lowest pressure drop, while the rectangular riblet surface achieved the highest particle deposition enhancement. They concluded that square ribs are an efficient and effective alternative for efficiency enhancement compared with triangular and circular ribs, but the flow drag still increased with a ratio of 9.8

compared with a plain surface. By reducing the pressure drop, the total efficiency ratio can still overwhelm the designed micro-structured surface discussed above. Overall, it is valuable and crucial to investigate more patterned surfaces and optimize the dimensions for higher deposition enhancement with a lower pressure drop.

To enhance particle deposition and minimize the resistance, nature traits can inspire the optimized shape of surface ribs (Bhushan 2009). Experimental and numerical results have shown that shark skin can effectively reduce fluid drag up to 9.9% in the turbulent flow regime (Bechert et al. 2000; Bechert et al. 1997; Deyuan et al. 2011). Dean and Bhushan (2010) found that riblets cause a shear stress reduction at the shark skin surface. The shark skin (called dermal denticles) has tooth-like ribs with longitudinal grooves, which resembles a semi-circular shape. The fluid drag was reduced because the amount of shark skin area exposed to the high-velocity flow reduced as the vorticity region separated from the skin surface. On the other hand, the reduction of drag on shark skin also prevents bio-organisms from fouling (Bhushan 2009). Liu et al. (2009) observed that fish scales remain clean in oil-polluted water. They created a low-adhesive superhydrophobic interface by using the fish slime. Their findings also implied a reduction in drag would help to resist particle residences on the surface, thus decrease the fouling effect. Another natural phenomenon is the lotus effect to let particles adhere to a surface. The edge of lotus leaves possesses a semi-circular hierarchical structure to deposit submicron particles downwind of the edge due to the effect of turbulent eddies. The surface also processes the effect of superhydrophobicity and self-cleaning to remove any contaminant particles when water droplets roll off (Bhushan and Her 2010; Nosonovsky and Bhushan 2008). Tree Leaves have been reported to remove large numbers of airborne particles and hence improve the environmental air quality (Beckett et al. 1998). From the above traits found in nature, the particle deposition enhancement

and drag reduction cannot occur simultaneously. Similar to fast-swimming sharks and fish, lower drag increases fluid flow at the skin and decreases flow resistance. However, a lower fluid drag will reduce particle settlement time, as the particles do not have sufficient response time to react with near-wall eddies. If a higher particle deposition enhancement occurs, suspended particles will more easily foul the surface. A low drag surface often equates with less fouling and better energy conservation with the surrounding fluid. An efficiency index that includes both factors will be applied to investigate different shape of surface ribs inspired by nature under different pitch-to-height ratio ( $p/e$ ).

Previous research on particle deposition does not indicate the best shape for surface ribs with a higher efficiency index. The shape of patterned surfaces are mostly focused on rectangular ribs for micro-sized particle deposition. The deposition mechanism of submicron particles is very different from their larger counterparts. The deposition mechanism of the micro-sized particle is related to the turbulent dispersion and inertial impaction, while deposition of submicron particles suspended in the fluid is subject to the mechanisms of turbulent dispersion effect and Brownian motion. In this study, we explored patterned surfaces in the shape of rectangular, triangular, semi-circular and open-circular. The best deposition efficiency index can be selected among these patterned surfaces and different deposition mechanisms are demonstrated. A deposition experiment for the semi-circular patterned surface under a fully developed flow field was then set up to validate the results under different particle sizes and  $p/e$ . Finally, a recommended patterned surface at a specific  $p/e$  will be suggested from the numerical simulation to increase the energy efficiency of the current particle removal device.

## 2. NUMERICAL SETUP AND METHODOLOGY

### 2.1 Geometries of Bioinspired Surface Ribs

The geometry of patterns was studied by a non-dimensional ratio, the pitch-to-height ratio ( $p/e$ ) in numerical simulation. The shape of semi-circular, open-circular, triangular and rectangular ribs are displayed in Figure 1(a), (b), (c) and (d). The length of the channel is 400 mm and the width of the channel is 20 mm. This dimension is consistent with the two-dimensional particle deposition benchmark cases by Tian and Ahmadi (2007) and Lu and Lu (2015). The radius of the semi-circular and open-circular patterns is 2 mm, and the height of the triangular and rectangular patterns is 2 mm. The base of the surface rib is 4 mm for all the cases. The  $p/e$  for different forms of patterned surface in Figure 1 is 3. A summation of parametric cases in this study is demonstrated in Table 1. In the mesh distribution, 11 inflation layers surround the wall of the surface ribs with the height of the first layer equal to  $5 \times 10^{-5}$  m. The mesh in the center of the channel increased to  $4 \times 10^{-4}$  m. The total number of mesh elements will be different between the different shapes of the surface ribs. A mesh dependence study has been performed to prove that the mesh distribution in this way can get solutions independent of mesh resolution.

Table 1. Summary of parametric cases

Shape of surface ribs	$p/e$	Particle size ( $\mu m$ )
Semi-circular	3, 4, 5 and 6	0.01, 0.1, 0.2, 0.5, 0.3, 1, 1.2 2, 3, 5, 8
Open-circular	3, 4, 5 and 6	0.01, 0.1, 0.2, 0.5, 0.3, 1, 1.2 2, 3, 5, 8
Triangular	3, 4, 5 and 6	0.01, 0.1, 0.2, 0.5, 0.3, 1, 1.2 2, 3, 5, 8
Rectangular	3, 4, 5 and 6	0.01, 0.1, 0.2, 0.5, 0.3, 1, 1.2 2, 3, 5, 8

### 2.2 Turbulent Flow Field with Discrete Phase Model

A set of Reynolds-averaged Navier-Stokes (*RANS*) equations were selected to model the

turbulent airflow interaction with particle motion. ANSYS Fluent 16.0 was used to solve the momentum equations as well as Lagrangian particle tracking. A Reynolds stress turbulent model (*RSM*) with velocity fluctuation can be a more precise model to predict and quantify the deposition mechanism compared with other two-equation turbulent models (Xu et al. 2019). The full equation of RSM can be written as Equation (1),

$$\begin{aligned} \frac{\partial}{\partial t} (\overline{\rho u_i' u_j'}) + \frac{\partial}{\partial x_k} (\overline{\rho u_k u_i' u_j'}) = & -\rho \left( \overline{u_i' u_k'} \frac{\partial u_j}{\partial x_k} + \overline{u_j' u_k'} \frac{\partial u_i}{\partial x_k} \right) + p \left( \frac{\partial u_i}{\partial x_j} + \frac{\partial u_j}{\partial x_i} \right) - \\ & 2\mu \frac{\partial \overline{u_i}}{\partial x_k} \frac{\partial \overline{u_j}}{\partial x_k} - \frac{\partial}{\partial x_k} [\overline{\rho u_i u_j u_k} + \overline{p u_i} \delta_{jk} + \overline{p u_j} \delta_{ik}] + \frac{\partial}{\partial x_k} \left[ \mu \frac{\partial}{\partial x_k} (\overline{u_i u_j}) \right] \end{aligned} \quad (1)$$

The random walk model was applied to reproduce the instantaneous velocity field that characterizes the turbulence eddy effect. The inlet mean velocity in our numerical case is 5 *m/s* and the properties of air are the same as the FLUENT material database. The Reynolds number based on average velocity and channel width was 6845. The boundary condition for channel walls was set to be no-slip and adiabatic. Regarding the conditions for the discrete phase model, the channel walls are set to “trap” particles and the inlet and outlet are set to “escape”. It assumed that the particles cannot resuspend if they attach to the channel walls, while the remaining particles that did not attach to walls will flow through the channel outlet. This assumption may be contradicted by the amorphous solid particles with weaker adhesive forces and thus more susceptible to particle resuspension. In our experiment, we used liquid aerosol (di-2-ethyl hexyl sebacate) with high adhesive force and there was no resuspension of particles after deposition. A fully developed turbulent inlet velocity was modeled with a 1/7<sup>th</sup> power law (Tian and Ahmadi 2007) as given in Equation (2) and (3).

$$U = \frac{8}{7} U_{mean} \left( \frac{y}{h/2} \right)^{1/7} \text{ for } 0 \leq y \leq \frac{h}{2} \quad (2)$$

$$U = \frac{8}{7}U_{mean} \left(\frac{h-y}{h/2}\right)^{1/7} \text{ for } \frac{h}{2} \leq y \leq h \quad (3)$$

The fully developed turbulence kinetic energy at the inlet is given as Equation (4) and (5).

$$k = \frac{\tau_w}{\rho\sqrt{C_\mu}} + \frac{y}{h/2} \left(0.002U_{free}^2 - \frac{\tau_w}{\rho\sqrt{C_\mu}}\right) \text{ for } 0 \leq y \leq \frac{h}{2} \quad (4)$$

$$k = \frac{\tau_w}{\rho\sqrt{C_\mu}} + \frac{h-y}{h/2} \left(0.002U_{free}^2 - \frac{\tau_w}{\rho\sqrt{C_\mu}}\right) \text{ for } \frac{h}{2} \leq y \leq h \quad (5)$$

The Fluent Lagrangian discrete phase model (DPM) was solved by Equation (6) to couple with the turbulent flow field. Zhao et al. (2011) suggested that Fluent Lagrangian DPM can be reliable to model Brownian diffusion on particle-laden turbulent airflow.

$$m_p \frac{d\vec{u}_p}{dt} = \vec{F}_{drag} + \vec{F}_{gravitation} + \vec{F}_{Brownian} + \vec{F}_{lift} \quad (6)$$

One-way coupling is used to assume that the airflow can affect the particle motion, but the inverse effect is disabled. The detailed expressions of particle drag force ( $F_{drag}$ ), Brownian motion force ( $F_{brownian}$ ), gravitational force ( $F_G$ ) and particle lift force ( $F_L$ ) are listed in Table 2. The particle drag force for micron-sized particles is dependent on different particle Reynolds number, which can be defined in Equation (7). Submicron particles tend to follow the flow field more quickly and, therefore, the local velocity of each particle can be considered as having the same local velocity of air.

$$Re_p = \frac{d_p |u - u_p|}{\nu} \quad (7)$$

Table 2. Particle force components

	Submicron particles ( $<1\mu m$ )	Micron-sized particles ( $>1\mu m$ )
Particle drag force	$\vec{F}_{drag} = \frac{18\mu}{d_p^2 \rho_p C_c}$ $C_c = 1 + \frac{2\lambda}{d_p} (1.257 + 0.4e^{-\left(\frac{1.1d_p}{2\lambda}\right)})$	$F_{drag} = \frac{18\mu}{\rho_p D_p^2} \frac{C_D Re_p}{24}$ $C_D = \frac{24}{Re_p} \text{ for } Re_p < 1$



---

	$C_D = \frac{24}{Re_p} (1 + 0.15Re_p^{0.687})$ <p style="text-align: center;">for <math>1 &lt; Re_p &lt; 400</math></p>
Brownian motion	$F_{Brownian} = \zeta \sqrt{\frac{\pi S_0}{\Delta t}}, \quad S_0 = \frac{216\rho_g \nu_g k_b T}{\pi^2 \rho_p^2 d_p^5 C_c}$
Gravitational force	$m_p g$
Lift force	(Saffman 1965)

---

The particle deposition velocity and relaxation time in the non-dimensional forms can be estimated by Equation (8) and (9). In the numerical simulation, 30000 particles were initially distributed with uniform concentration within 30 wall units at  $x=0.2$  m. From 0 to 0.055 s, the particles were not released until the flow was fully developed. Here, we used a constant particle concentration to simulate the deposition number in a quasi-equilibrium condition ( $N_d/t_d^+$ ).

$$u_d^+ = \frac{N_d/t_d^+}{N_0/y_0^+} \quad (8)$$

$$\tau^+ = \frac{Sd^2 u^{*2}}{18\nu^2} C_c \quad (9)$$

### 3. EXPERIMENTAL VALIDATION FOR THE SEMI-CIRCULAR PATTERNED SURFACE

Experiments were also conducted in this study to validate the numerical results. As shown in Figure 2, a wind tunnel was set up to provide a fully developed turbulent channel flow with a dimension of 20 mm in height and 200 mm in width (Fu et al. 2014). Monodispersed NaCl particles at a certain particle size were generated by an aerosol generator (TSI 3475, TSI Incorporated, USA). All particles are spherical, and the particle density is 912 kg/m<sup>3</sup>. In order to measure the particle concentration at the size of 2.5  $\mu\text{m}$  and 0.5  $\mu\text{m}$  separately, a GRIMM particle spectrometer (Model 1.108, Technik GmbH & Co, KG) and a Scanning Mobility Particle Sizer (Model 3080, TSI

Incorporated, USA) were used for micron-sized and submicron particles above the patterned surface. The minor figure at the right bottom side is the smooth surface and semi-circular patterned surface at the height of 2000  $\mu\text{m}$ . The particle size measured by the TSI Model 3080 and GRIMM Model 1.108 are geometric size. The TSI Model 3080 program differentiates the particle sizes based on their electrical mobility, which closely matches particles' geometric diameter. The GRIMM Model 1.108 monitors the particle size based on the optical laser technology; the program outputs the size similar to the geometric size. Under the microscope, we visualize the real geometric size of deposited particles. Therefore, the particle sizes obtained from the experiment are geometric size.

The experimental deposition velocity was tested and compared using a smooth surface and a semi-circular shape at  $p/e=3$ ,  $p/e=4$ ,  $p/e=5$  and  $p/e=6$ . Before calculating the particle deposition velocity, the deposited particle number was analyzed by using the total volume of deposited aerosol. The liquid aerosol droplets deform after they deposit on the surface. The volume of each aerosol needs to be calculated based on the contact angle and contact area. The aerosol three-phase contact angle on the patterned surface was measured by a Biolin Theta Contact Angle Meter, which is around  $23^\circ$  to  $25^\circ$ . As illustrated in Figure 3, the total volume of this cap can be viewed as identical to the volume of the original droplet. The mathematical equation to calculate the spherical cap is displayed in Equation (10).

$$V_{cap} = \frac{2}{3}\pi R_s^3(1 - \cos\alpha) - \frac{1}{3}\pi R_s^3 \sin^2\alpha \cos\alpha = \frac{1}{3}\pi R_s^3(2 - 3\cos\alpha + \cos^3\alpha) \quad (10)$$

In Equation (10),  $\alpha$  is the three-phase contact angle and  $R_s$  is the radius of the larger sphere in Figure (3). From Equation (10),  $R_s$  can be expressed as in Equation (11).

$$R_s = V_{cap}^{1/3} \left[ \frac{\pi}{3} (2 - 3\cos\alpha + \cos^3\alpha) \right]^{-1/3} \quad (11)$$

The contact area of the circle can be expressed by Equation (12).

$$A_{s-l} = \pi r_s^2 = \pi (R_s \sin\alpha)^2 \quad (12)$$

Substituting Equation (11) with Equation (12), the contact area of the planar surface and volume of the larger aerosol can be found using Equation (13) and (14).

$$A_{s-l} = \pi V_{cap}^{2/3} \left[ \frac{\pi}{3} (2 - 3\cos\alpha + \cos^3\alpha) \right]^{-2/3} \sin^2\alpha \quad (13)$$

$$V_{cap} = \left( \frac{A_{s-l}}{\pi \left[ \frac{\pi}{3} (2 - 3\cos\alpha + \cos^3\alpha) \right]^{-2/3} \sin^2\alpha} \right)^{3/2} \quad (14)$$

In the particle deposition experiment, some of the aerosols will inevitably coalesce over time. Following this, small monodisperse aerosols coalesce into large droplets. Here, we applied Equation (15) to calculate the number of deposited monodispersed aerosols in a larger droplet.

$$N_d = \frac{V_{cap}}{\frac{4}{3} \pi \left(\frac{d_p}{2}\right)^3} \quad (15)$$

The experimental particle deposition velocity to a surface is defined as Equation (16).

$$u_d^+ = \frac{J}{n_0 \times u^*} = \frac{\text{particle number deposited}/(\text{Area} \cdot t_d)}{\text{particle number}/\text{volume} \times u^*} \quad (16)$$

In Equation (16),  $J$  is the particle flux to the patterned surface,  $n_0$  is the particle concentration above the patterned surface. The deposition duration for 2.5  $\mu\text{m}$  particles is 600 s, and the deposition duration for 0.5  $\mu\text{m}$  particles is 5400 s. The particle concentration of 2.5  $\mu\text{m}$  and 0.5  $\mu\text{m}$  is around  $1 \times 10^9 \text{ \#/m}^3$  and  $4 \times 10^9 \text{ \#/m}^3$ . The particle concentration for each experiment varied in a small range because the total flow rate from the nitrogen cylinder fluctuated.

The flow rate at the outlet of the aerosol generator was around 3.5 to 4.0 L/min and the particle-particle interaction would not happen. The experimental deposition velocity is calculated by Equation (17). This equation is a function of the visualized radius in the microscope ( $r_s$ ), aerosol contact angle ( $\alpha$ ), particle size ( $d_p$ ), visualized area under the microscope ( $A_d$ ), deposition duration ( $t_d$ ), particle number concentration ( $n_0$ ) and friction velocity ( $u^*$ ).

$$u_d^+ = \frac{J}{n_0 \times u^*} = \frac{2r_s^3(2 - 3\cos\alpha + \cos^3\alpha)}{d_p^3 \times \sin^3\alpha \times A_d \times t_d \times n_0 \times u^*} \quad (17)$$

The friction velocity in a fully-developed channel flow can be calculated by using the square root of wall shear stress divided by fluid density in Equation (18). The friction velocity describes the influence of shear-related motion to the particle diffusion and dispersion.

$$u_f = \sqrt{\frac{\tau_w}{\rho}} = \sqrt{-\frac{h}{2\rho} \frac{dp}{dx}} \quad (18)$$

where  $h=20$  mm and is the height of the channel, and  $dp/dx$  is the pressure drop per length in the downstream direction. The total pressure before and after the patterned surface is 13 Pa and 8 Pa while the velocity at the centerline of the channel is 5 m/s. The friction velocity can be calculated as 0.52 m/s. Figure 4(a) and (b) displayed the photos for 0.5  $\mu\text{m}$  particles before and after deposition. The blue circle in Figure 4(b) represents coalesced particles after the deposition. However, the other black spots are defects that were initially on the surface. The particle radius in Figure 4(b) was identified by the Nikon microscope software. The comparison of non-dimensional deposition velocity for different  $p/e$  of a semi-circular shape between the experiment and numerical simulation is displayed in Figure 5. Figure 5(a) and (b) show the results for the particle size of 2.5  $\mu\text{m}$  and 0.5  $\mu\text{m}$ . It can be clearly observed that there is an optimal  $p/e$  for different particle sizes. At this optimal  $p/e$ , the non-dimensional deposition velocity agrees well between the experiment

and numerical simulation. At other  $p/e$ , the experimental and numerical results follow a similar trend from  $p/e$  of 3 to 6. Therefore, the submicron and micron-sized particle deposition on a patterned surface at different  $p/e$  was validated.

## **4. NUMERICAL RESULTS AND DISCUSSION**

### **4.1 Comparison of Particle Deposition Velocity Among Different Patterned Surfaces**

In this section, we investigate the performance of a smooth channel, a channel with semi-circular patterns, a channel with open-circular patterns, a channel with rectangular patterns and a channel with triangular patterns as shown in Figure 6. It can be clearly observed that the deposition velocities have a “V-shape” variation for the particle deposition on a smooth surface for a wide range of particle sizes. Figure 6 (a), (b), (c) and (d) compare the particle deposition velocity under the  $p/e$  of 3, 4, 5 and 6 for the semi-circular, open-circular, rectangular and triangular patterned surfaces. In general, the particle deposition on a patterned surface is greatly enhanced when compared with a smooth channel for broad sizes of particles. This can be explained by the disturbance of turbulence kinetic energy at the near-wall regions and separation flow mechanism between two consecutive patterns. The “V” curves of particle deposition are dramatically weakened by a semi-circular, rectangular rib and triangular micropatterned surface. There still exists a “V” curve for the open-circular patterned surface, however, the trough around the non-dimensional relaxation time of 0.1 appears flat compared with the clean channel results. If a qualitative comparison is made between the smooth surface and patterned surface, the particle deposition velocities of smooth and patterned surfaces are similar at the inertia-impaction regime

(right side of the curve). The magnitude of deposition velocity for a patterned surface increased 10 times at the diffusional deposition regime (left side of the curve), and 1000 times at the diffusional impaction regime (middle range of the curve). Due to the tremendous enhancement by the patterned surface at the middle range of the curve compared with the left and right side of the curve, the trough of the “V” curve disappears in Figure 6 for patterned surface. At each  $p/e$ , the semi-circular and triangular patterned surface achieves the highest deposition velocity, while the open-circular pattern has the lowest deposition velocity. This is reasonable because the turbulent kinetic energy at the near-wall regions was enhanced by obstacles in the flow, while the open-circular patterned surface did not have any obstacles in the flow direction. Although the open-circular patterned surface has the worst performance among all the other patterned surfaces, the particle deposition number still overwhelms the smooth channel results.

## **4.2 Comparison of Efficiency Index Among Different Patterned Surfaces**

Although the semi-circular and triangular patterned surfaces could significantly enhance particle deposition, more fluid drag is also induced by these obstacles. The fish slime composition inspires the open-circular patterned surface. Liu et al. (2009) reported that the fish slime composition (or mucus) causes a reduction in drag when the fishes swim. Their findings also implied a reduction in drag would help to resist particle residence on the surface, thus decrease the fouling effect. From the above study, it is normal that the particle deposition velocity of an open-circular pattern has the worst performance, but the overall performance by combining the deposition enhancement and pressure loss should be considered. A dimensionless factor, efficiency index, is applied to compare the deposition and fluid performance of the four micro-patterns (Lu

and Lu 2015). The efficiency index of the patterned surface is defined with Equation (19).

$$\eta = \frac{u_{d-rough}}{u_{d-smooth}} \cdot \frac{f_{d-smooth}}{f_{d-rough}} \quad (19)$$

where  $u_{d-rough}$  and  $u_{d-smooth}$  are the particle deposition velocities of a patterned surface and smooth surface respectively, and  $f_{d-rough}$  and  $f_{d-smooth}$  are the friction factors for a patterned surface and smooth surface respectively. The friction factor is defined in Equation (20).

$$f = \frac{\Delta P}{\Delta L} \frac{D_h}{2\rho_a U_{ave}^2} \quad (20)$$

where  $\Delta P$  is the total pressure drop between the inlet and outlet, and  $\Delta L$  is the duct length.  $D_h$  is the hydraulic diameter defined by Equation (21).

$$D_h = \frac{4A}{pe} \quad (21)$$

Figure 7 shows the pressure drop along the channel for a patterned surface at various  $p/e$  from numerical simulation. The pressure drop for a smooth surface is 5.95 Pa. The triangular patterned surface has the largest pressure drop and the open-circular patterned surface has the lowest pressure drop. For triangular, semi-circular and rectangular patterned surfaces, the pressure drop increased as the  $p/e$  increased. As for the open-circular pattern, a larger  $p/e$  results in a lower pressure drop in the channel. Figure 8(a), (b), (c) and (d) illustrate the efficiency index for different patterned surfaces and pitch-to-height ratio. It can be seen for different  $p/e$ , the semi-circular patterned surface overwhelms the other micro-patterns and achieves the best efficiency index. The triangular patterned surface has the lowest overall performance because the flow resistance induced by the triangular pattern counteracts the enhancement of particle deposition. The efficiency index reaches the maximum at the middle range of the curve, while the efficiency index decreases at the left and

right side of the curve. This indicates the patterned surface can significantly increase the efficiency index for the particles at the diffusional impaction regime.

### 4.3 Deposition Mechanism for Open-circular Patterned Surface

The turbulence kinetic energy contour of an open-circular patterned surface is shown and displayed in Figure 9. The turbulence kinetic energy between the cavity decreases as the  $p/e$  increases from Figure 9(a) to Figure 9(d). Among all the different pitch-to-height ratios, there is a recirculation region inside each open-circular pattern. The turbulence kinetic energy contour, together with the recirculation flow inside the open-circular pattern, provide a possible explanation on why the  $p/e$  of 3 has the best particle deposition enhancement. Once the submicron particles flow into the trough with the recirculation flow, the particles are trapped by the high-turbulence-kinetic-energy region. The momentum energy of submicron particles cannot overwhelm the turbulence kinetic energy created by the patterned surface, which results that the submicron particles diffuse through the near-wall boundary layers and then deposit on the surface.

Different deposition locations of submicron particles are illustrated in Figure 10. The color legends in Figure 10, 11, 13 and 15 represent the particle velocity magnitude (m/s), and dot's colors in the figures show different particle velocity. The red dots represent the particles with high-velocity magnitude, and the blue dots represent the particles with low-velocity magnitude. At  $t=0.006$  s, only some of the particles flow into the right side of the open-circular pattern. Because the maximum turbulence kinetic energy occurs at the downward side of the open-circular cavity, ultrafine particles will be diffused to the surface. As more particles flow into the open-circular pattern (from  $t=0.006$  s to  $t=0.01$  s), the particle deposition location only occurs at the downward side of the open-circular pattern and particles disperse away from the surface at the bottom of the



pattern. From Figure 9, there is a small blue region in the turbulence kinetic contour near the bottom of the open-circular pattern; thus, the particles are not easily trapped by the fluid kinetic energy. At  $t=0.011$  s and  $t=0.012$  s, particles follow the flow pattern without colliding with the surface at the bottom and are upstream of the open-circular pattern. It can be seen in Figure 10(d), particles only deposit at the edge of the open-circular pattern where the turbulence kinetic energy is enhanced. Figure 11 shows the particle deposition location for  $2.5\ \mu\text{m}$  particles at different time steps. From  $t=0.006$  s to  $t=0.012$  s, a substantial number of particles deposit on almost the whole surface. The primary mechanism for a particle size larger than  $1\ \mu\text{m}$  is inertial impaction. The gravity sedimentation forced particles to deposit directly on the surface without following the recirculation flow. The particle deposition locations are obvious by comparing the particle deposition locations in Figure 10 and Figure 11.

## **4.4 Comparison of Particle Deposition Mechanism Among Different Patterned Surfaces**

The particle deposition mechanism for different types of patterns have been proposed in an attempt to explain why the shape of semi-circular and triangular ribs have the best deposition enhancement compared with a rectangular rib. The turbulence kinetic energy contour and flow patterns have been compared in Figure 12(a) and (b) for the triangular and rectangular patterned surface at the  $p/e$  of 6. There is a high-turbulence-kinetic-energy region at the top of the cavity for both patterns. The high-turbulence-kinetic-energy zone (red region) in Figure 12(a) covers the whole cavity. Inside this cavity, a saddle point surrounded by a recirculation flow appears upstream, then the flow separates to form a swirl node downstream of the cavity. In Figure 12(b), the high-turbulence-kinetic-energy zone only covers half of the cavity. Two separate swirl flows exist in a

large closed-loop recirculation area. This difference in flow patterns and turbulence kinetic energy yields possible reasons for the particle deposition mechanisms in Figure 13 and Figure 14.

The Lagrangian particle tracking results at different time steps on the rectangular and triangular patterned surface are displayed in Figure 13 and Figure 14. From Figure 13(a) to (d), most of the particles flow into the upstream and downstream of the cavity. However, few particles are entrained in the upstream region from Figure 13(a) to Figure 13(d). Most of the particles in Figure 13(d) tend to accumulate at the downstream region of the cavity. The difference in deposition mechanisms between Figure 13(d) and Figure 14(d) give a hint to explain the deposition velocity of triangular ribs being much higher than for rectangular ribs. From Figure 14(a) to (d), the particles filled up the upstream and downstream regions between the triangular ribs. There exists a large recirculation zone in Figure 12(a) and (b) for both cases. The range of the recirculation flow covered the upstream region in Figure 12(a), while the recirculation flow did not cover the left corner of the cavity. Also, there is a low-turbulence-kinetic-energy region at the left corner in Figure 12(b), which leads to the loss of particles being trapped in the upstream region. The flow patterns and turbulence kinetic energy of the semi-circular patterned surface have been discussed in (Xu et al. 2019). The particle deposition mechanisms for semi-circular and triangular patterns are similar, and this is the reason why the deposition velocity curves for semi-circular and triangular patterns in Figure 6 are very similar. However, the semi-circular patterned surface suffers a lower pressure drop compared with the triangular patterned surface based on Figure 7. The efficiency index of the semi-circular patterned surface is higher than the triangular patterned surface. Even though the open-circular pattern obtains a much lower pressure drop compared with all the other shapes, the particle deposition velocity is much lower. By considering the above factors, the semi-circular patterned surface has the best efficiency index compared with the

triangular, rectangular and open-circular patterned surfaces.

## CONCLUSIONS

Particle deposition enhancement by various patterned surfaces (rectangular, triangular, semi-circular and open-circular) are presented in this work by using the Reynolds stress turbulent model and Lagrangian particle tracking. The deposition mechanisms of different particle sizes from ultrafine, submicron to micro-sized particles are studied and compared numerically. The numerical simulation results were compared and validated with the experimental deposition velocity. The variance of the particle deposition velocity follows a “V” curve for a smooth channel in the size range of 0.01 to 8  $\mu m$ . When the patterned surface has been added into the turbulent flow, the “V” curves of particle deposition are dramatically weakened. This is because the particle deposition at the submicron range has a much better deposition enhancement (nearly 1000) compared with ultrafine and micron-sized particles. The enhancement ratio at ultrafine and micron-sized particles is below 10 times. When different pitch-to-height ratios ( $p/e=3, 4, 5$  and 6) are considered for the open-circular surface, the  $p/e$  of 3 has the best particle deposition enhancement. Although the patterned surface can be proven to have higher particle deposition velocity compared with smooth channels, the pressure drop increases at the same time. An overall performance in terms of efficiency index of the different patterned surfaces has been compared to indicate the best shape to be used in the air cleaners. The semi-circular gets the highest efficiency index compared with other patterned surfaces for different  $p/e$ . A maximum deposition enhancement of 5009 can be reached at the  $p/e$  of 4 for the semi-circular patterns and a maximum efficiency index of 1137 at the  $p/e$  of 3 is obtained by considering the deposition enhancement as well as pressure drop increase. Thus, the semi-circular patterned surface can be developed as a

surface treatment method for current particle removal devices.

## REFERENCES

- Bechert DW, Bruse M, Hage W (2000). Experiments with three-dimensional riblets as an idealized model of shark skin. *Experiments in Fluids*, 28:403-412.
- Bechert DW, Bruse M, Hage W, Meyer R (1997). Biological surfaces and their technological application-laboratory and flight experiments on drag reduction and separation control, Paper presented at the 28th Fluid Dynamics Conference, CO, USA.
- Beckett KP, Freer-Smith PH, Taylor G (1998). Urban woodlands: their role in reducing the effects of particulate pollution. *Environmental Pollution*, 99:347-360.
- Bhushan B (2009). Biomimetics: lessons from nature—an overview. *The Royal Society*, 367:1445-1486.
- Bhushan B, Her EK (2010). Fabrication of superhydrophobic surfaces with high and low adhesion inspired from rose petal. *Langmuir*, 26:8207-8217.
- Dean B, Bhushan B (2010). Shark-skin surfaces for fluid-drag reduction in turbulent flow: a review. *Philosophical Transactions of the Royal Society of London A: Mathematical, Physical and Engineering Sciences*, 368:4775-4806.
- Deyuan Z, Yuehao L, Huawei C (2011). Application and numerical simulation research on biomimetic drag-reducing technology for gas pipelining. *Oil Gas-Eur Mag*, 37:85-90.
- Fu SC, Leung WT, Chao CY (2014). Detachment of droplets in a fully developed turbulent channel flow. *Aerosol Science and Technology*, 48:916-923.
- Ji JH, Bae GN, Kang SH, Hwang J (2003). Effect of particle loading on the collection performance of an electret cabin air filter for submicron aerosols. *Journal of Aerosol Science*, 34:1493-

1504.

Liu M, Wang S, Wei Z, Song Y, Jiang L (2009). Bioinspired design of a superoleophobic and low adhesive water/solid interface. *Advanced Materials*, 21:665-669.

Lu H, Lu L (2015). Effects of rib spacing and height on particle deposition in ribbed duct air flows. *Building and Environment*, 92:317-327.

Nosonovsky M, and Bhushan B (2008). Multiscale dissipative mechanisms and hierarchical surfaces: friction, superhydrophobicity, and biomimetics. Germany: Springer Science & Business Media.

Saffman PG (1965). The lift on a small sphere in a slow shear flow. *Journal of Fluid Mechanics*, 22:385-400.

Suh YJ, Kim SS (1996). Effect of obstructions on the particle collection efficiency in a two-stage electrostatic precipitator. *Journal of Aerosol Science*, 27:61-74.

Tian L, Ahmadi G (2007). Particle deposition in turbulent duct flows—comparisons of different model predictions. *Journal of Aerosol Science*, 38:377-397.

Xu H, Fu SC, Leung WT, Lai TW, Chao CY (2020). Enhancement of submicron particle deposition on a semi-circular surface in turbulent flow. *Indoor and Built Environment*, 29:101-116.

Zhao B, Chen C, Lai AC (2011). Lagrangian stochastic particle tracking: further discussion. *Aerosol Science and Technology*, 45:901-902.

## Figure captions

Figure 1. Bioinspired patterned surfaces for particle deposition: (a) Semi-circular ribs (b) Open-circular (c) Triangular ribs (d) Rectangular ribs

Figure 2. Experimental setup

Figure 3. Mathematical illustration of spherical cap on a flat surface

Figure 4. Deposition photos for the 0.5  $\mu\text{m}$  particles (a) before deposition (b) after deposition

Figure 5. Comparison of non-dimensional deposition velocity under different  $p/e$  between experiment and numerical simulation at the particle size of: (a) 2.5  $\mu\text{m}$  (b) 0.5  $\mu\text{m}$

Figure 6. Particle deposition velocity under different pitch-to-height ratios: (a) 3 (b) 4 (c) 5 and (d) 6

Figure 7. Pressure drop (Pa) for patterned surface under different pitch-to-height ratio

Figure 8. Efficiency index for different patterned surface under different pitch-to-height ratios: (a) 3 (b) 4 (c) 5 and (d) 6

Figure 9. Turbulence kinetic energy contour for open-circular patterned surface at the pitch-to-height ratio of (a) 3 (b) 4 (c) 5 and (d) 6

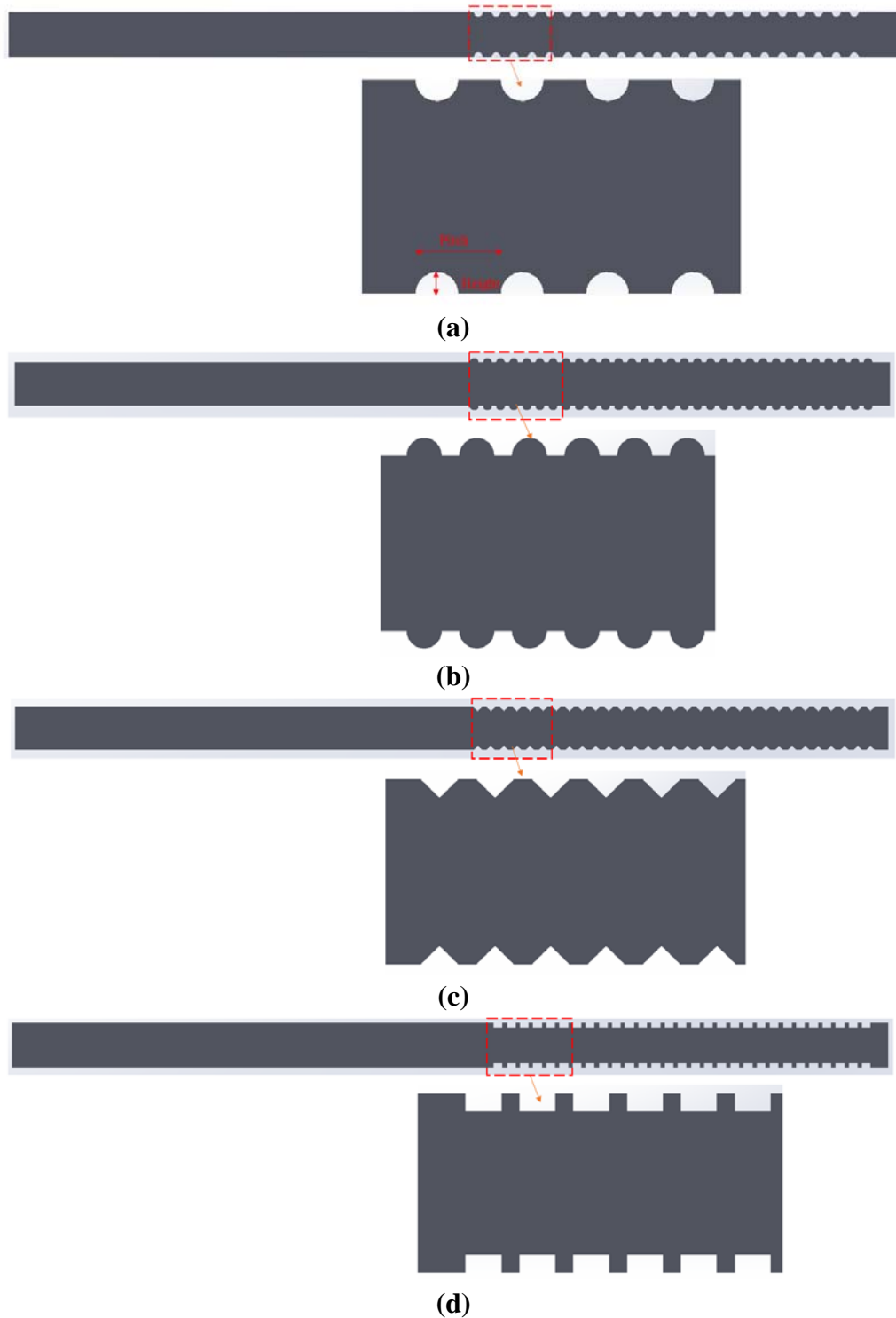
Figure 10. Deposition location for 0.5  $\mu\text{m}$  particles at the timestep of (a) 0.006 s (b) 0.008 s (c) 0.01 s (d) 0.012 s

Figure 11. Deposition location for 2.5  $\mu\text{m}$  particles at time step of (a) 0.006 s (b) 0.008 s (c) 0.01 s (d) 0.012 s

Figure 12. Turbulent kinetic energy for (a) triangular and (b) rectangular shapes at the  $p/e$  of 6

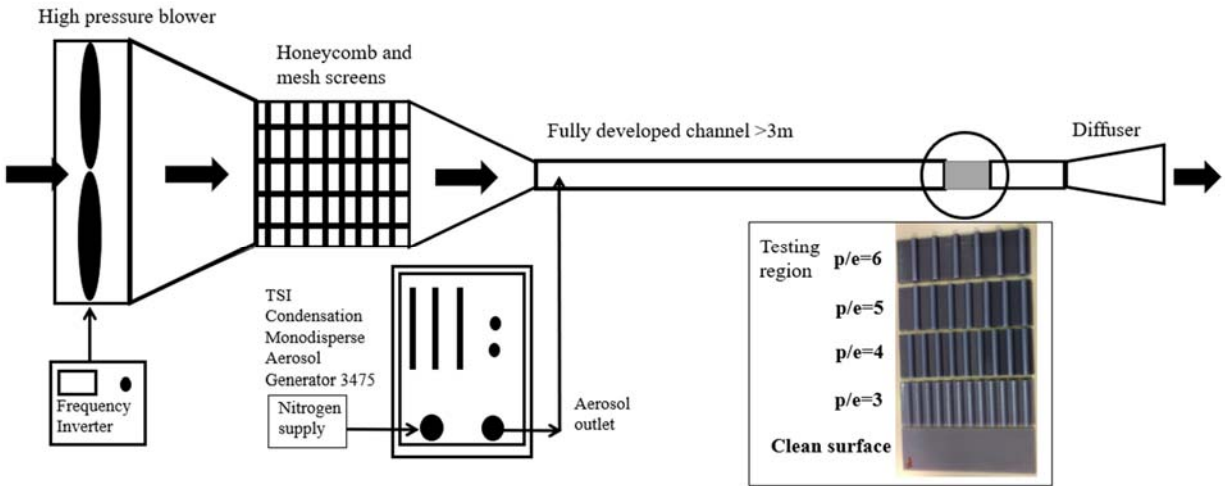
Figure 13. Lagrangian particle tracking results on the rectangular patterned surface at the time step of (a) 0.007 s (b) 0.009 s (c) 0.011 s and (d) 0.013 s

Figure 14. Lagrangian particle tracking results on the triangular patterned surface at the time step of (a) 0.005 s (b) 0.006 s (c) 0.007 s and (d) 0.008 s



**Figure 1. Bioinspired patterned surfaces for particle deposition: (a) Semi-circular ribs (b) Open-circular (c) Triangular ribs (d) Rectangular ribs**





**Figure 2. Experimental setup**

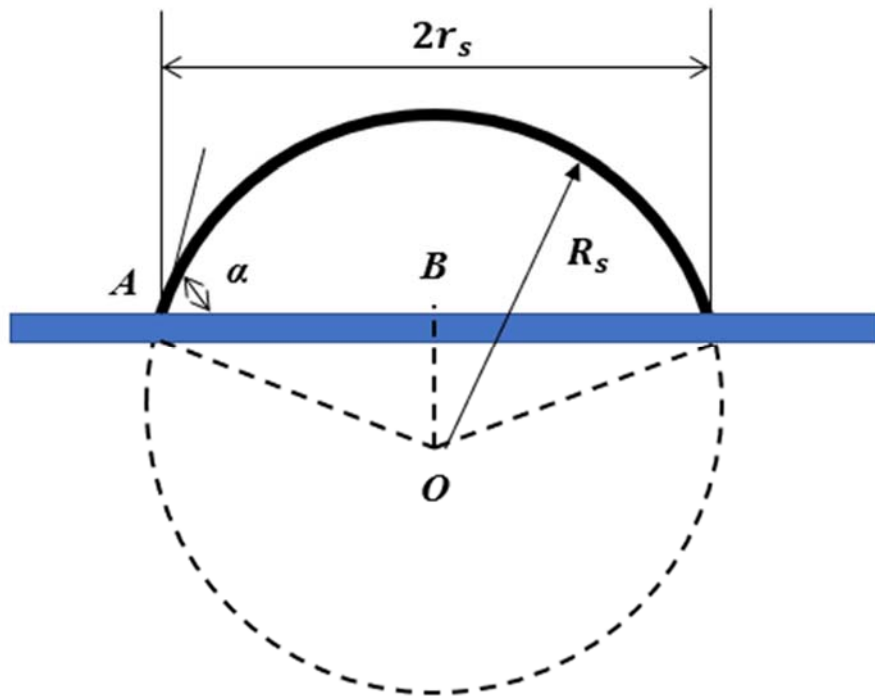
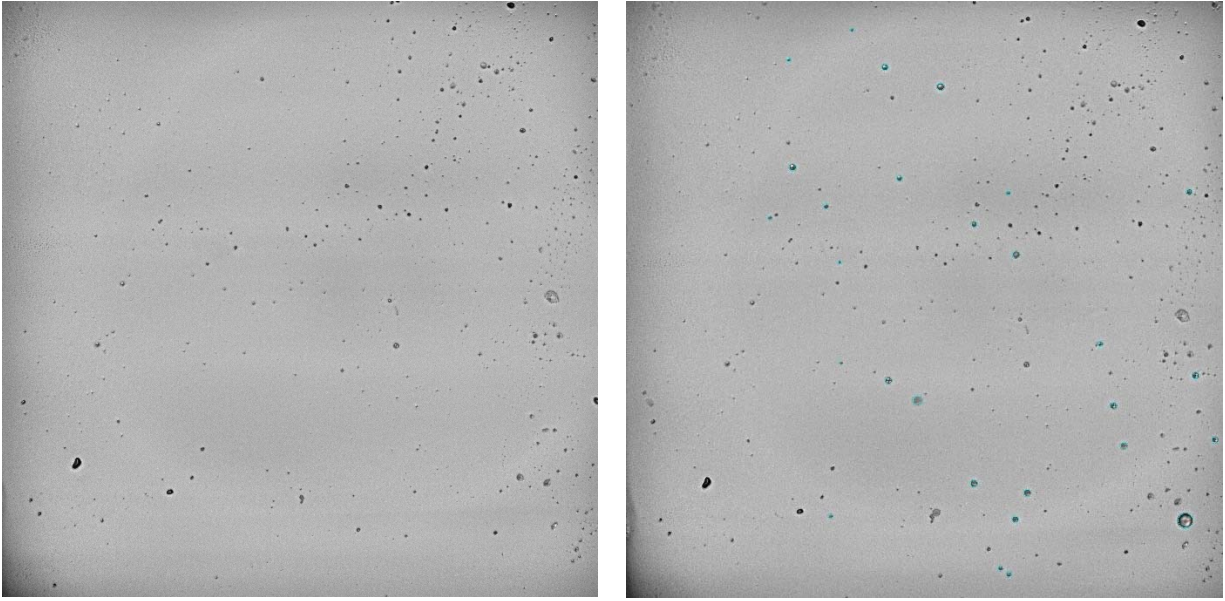


**Figure 3. Mathematical illustration of spherical cap on a flat surface**



(a)

(b)

**Figure 4. Deposition photos for the 0.5  $\mu\text{m}$  particles (a) before deposition (b) after deposition**

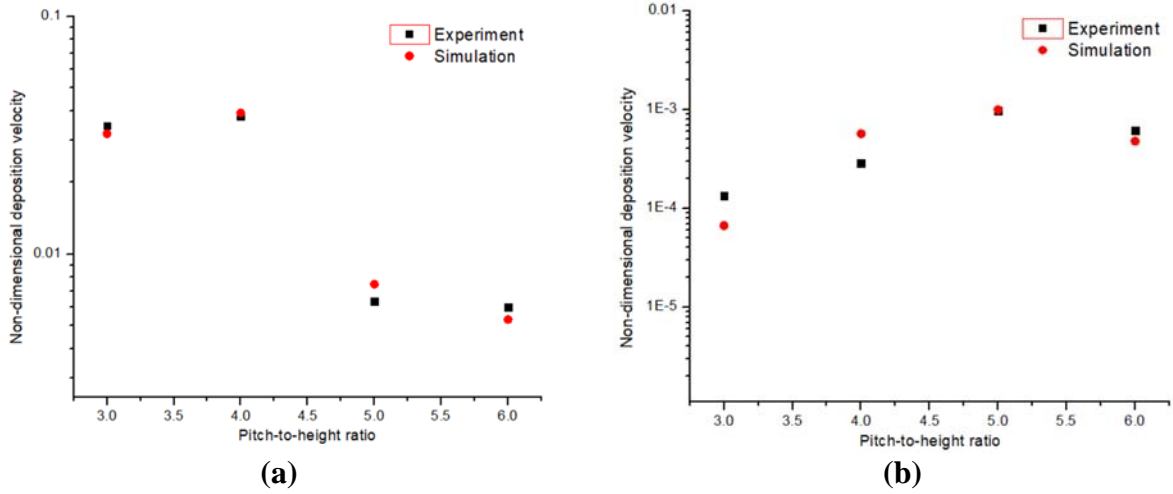


**Figure 5. Comparison of non-dimensional deposition velocity under different  $p/e$  between experiment and numerical simulation at the particle size of: (a) 2.5 μm (b) 0.5 μm**

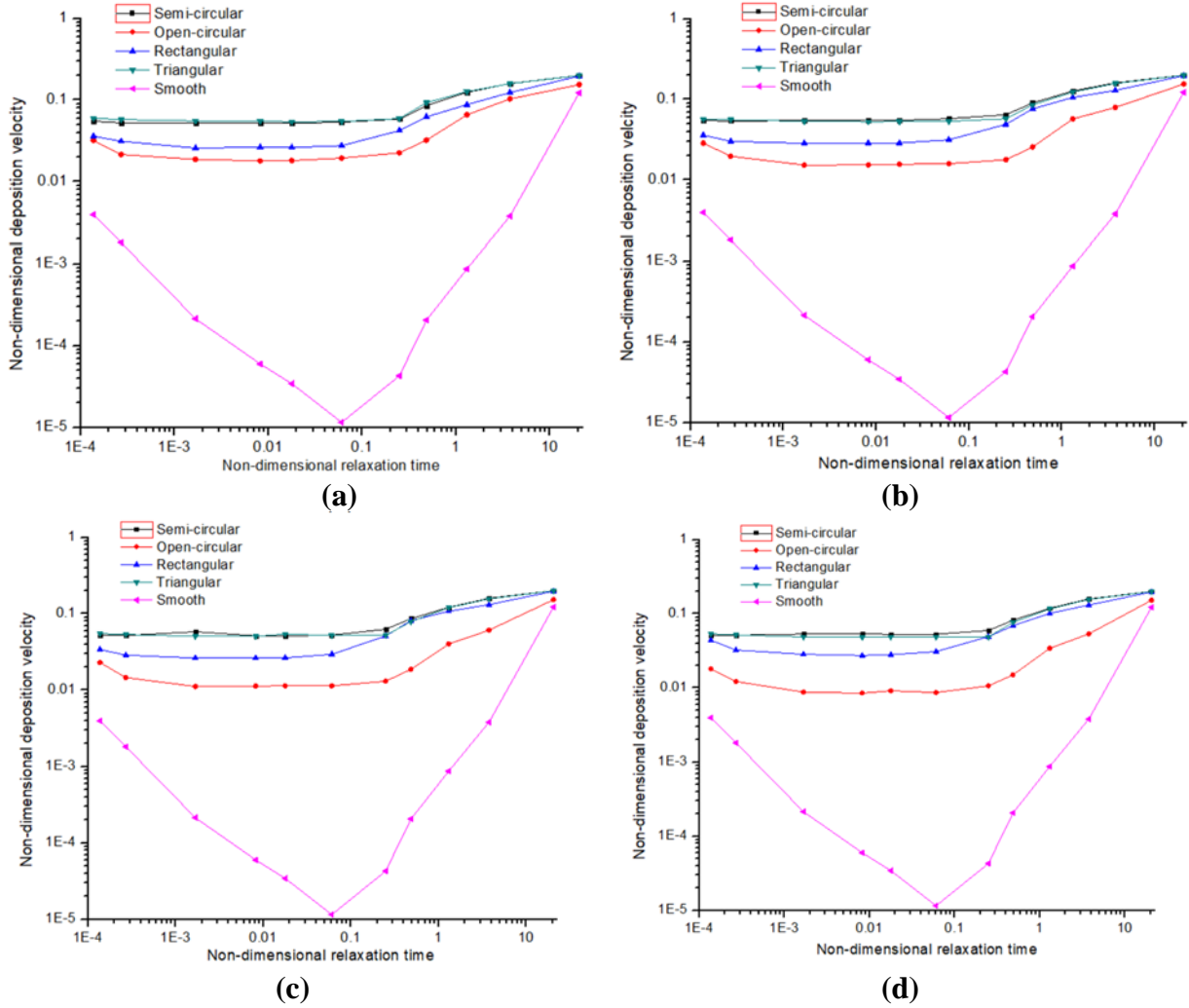


**Figure 6. Particle deposition velocity under different pitch-to-height ratios: (a) 3 (b) 4 (c) 5 and (d) 6**

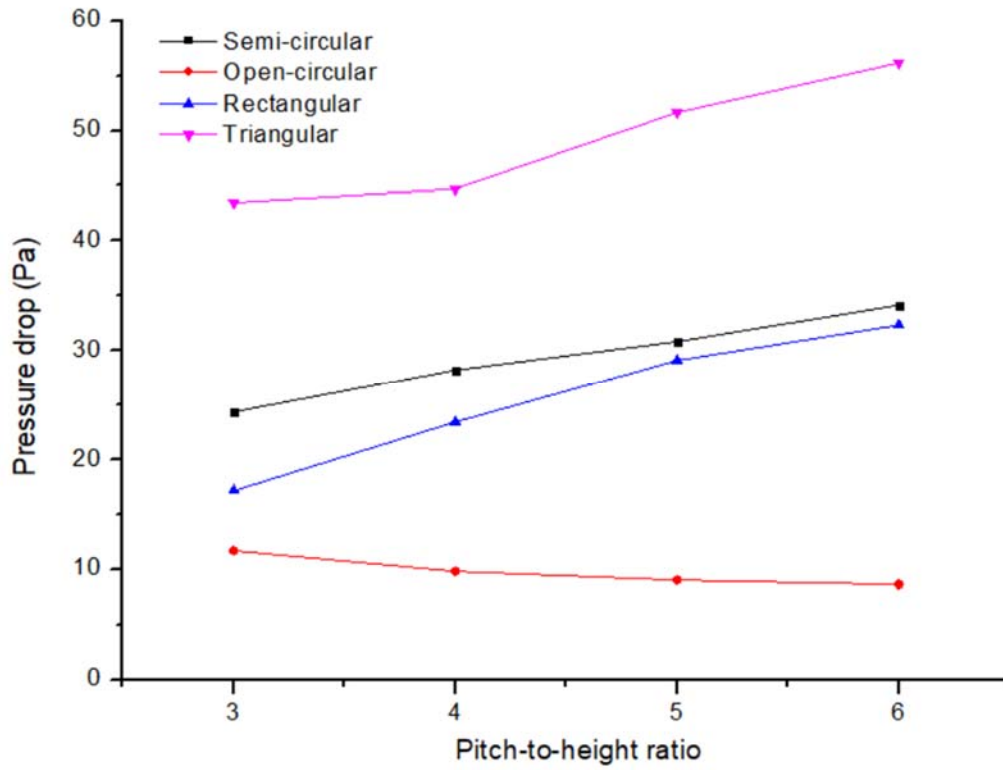


**Figure 7. Pressure drop (Pa) for patterned surfaces under different pitch-to-height ratio**

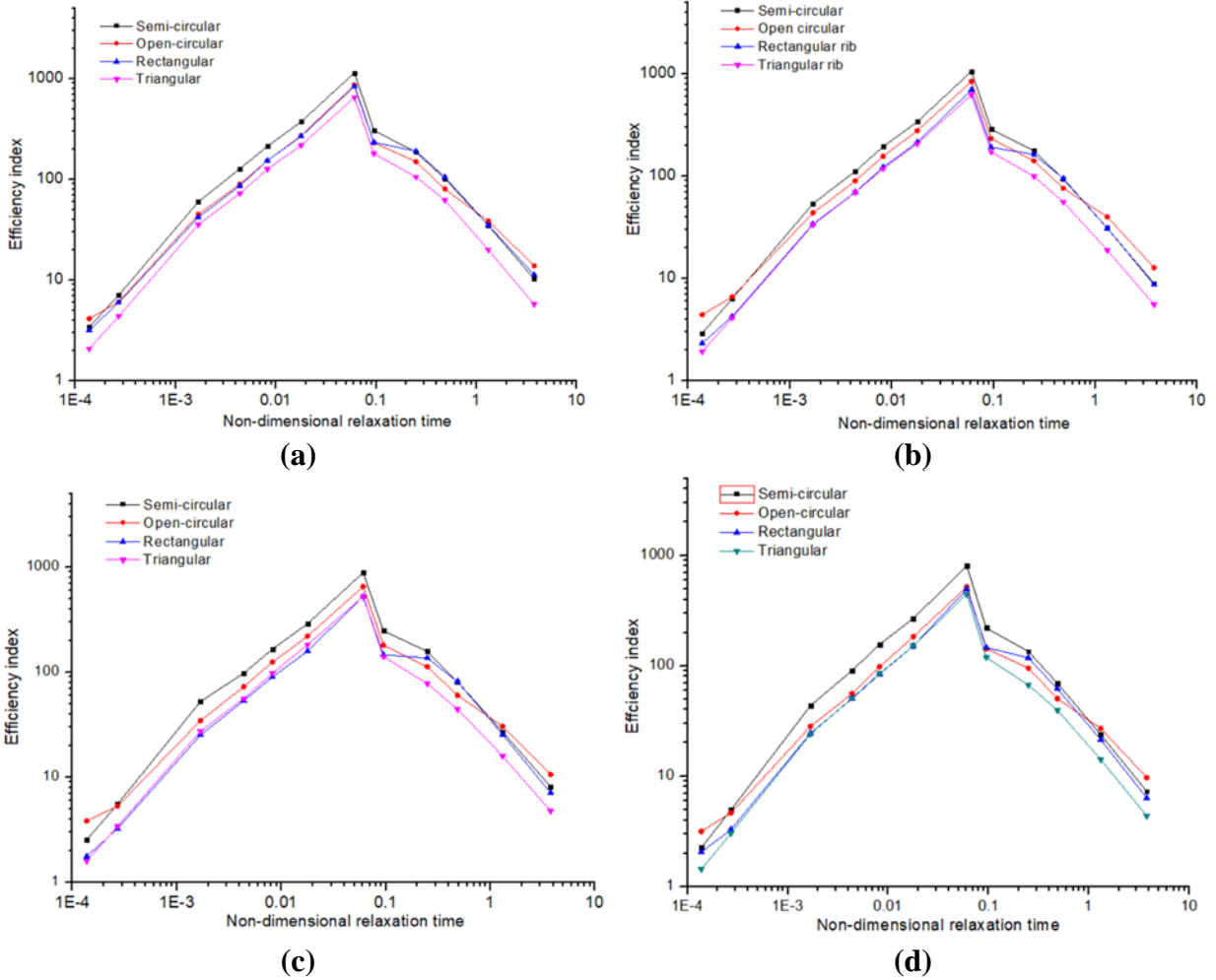


**Figure 8. Efficiency index for different patterned surfaces under different pitch-to-height ratios: (a) 3 (b) 4 (c) 5 and (d) 6**

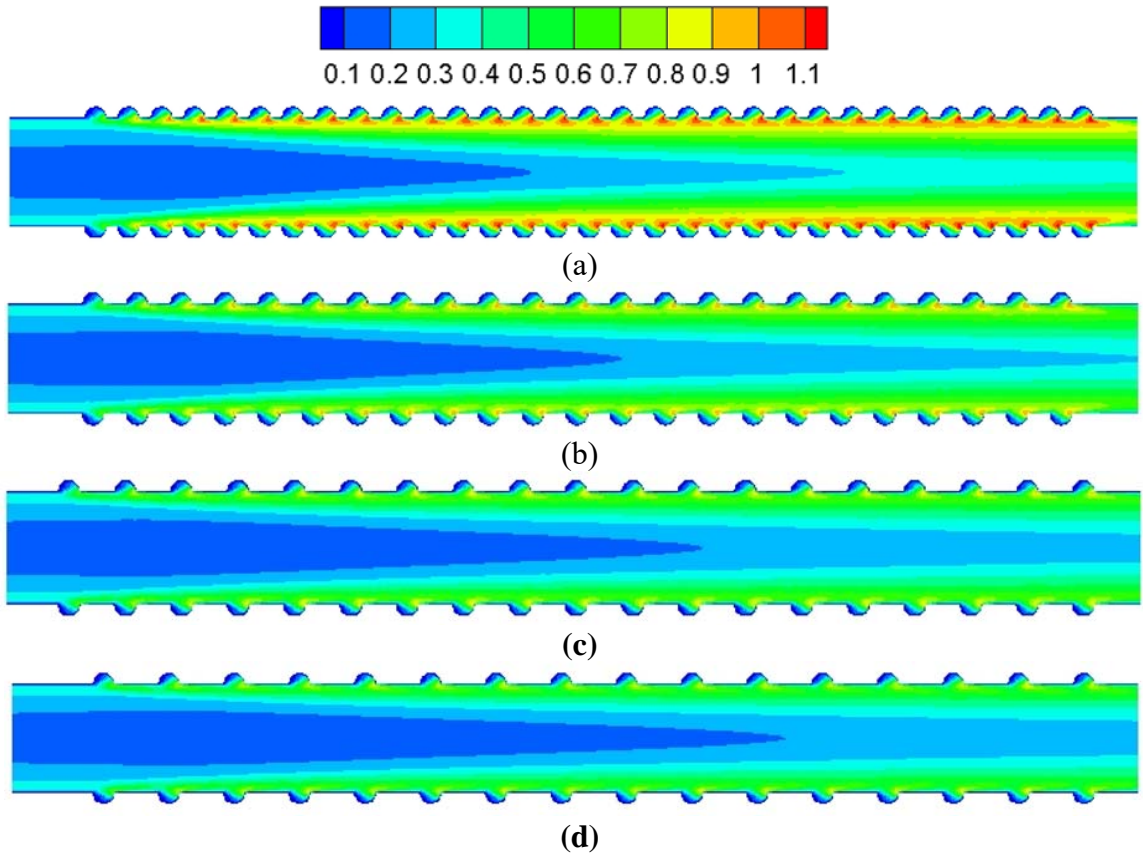


**Figure 9. Turbulence kinetic energy contour for open-circular patterned surface at the pitch-to-height ratio of (a) 3 (b) 4 (c) 5 and (d) 6**



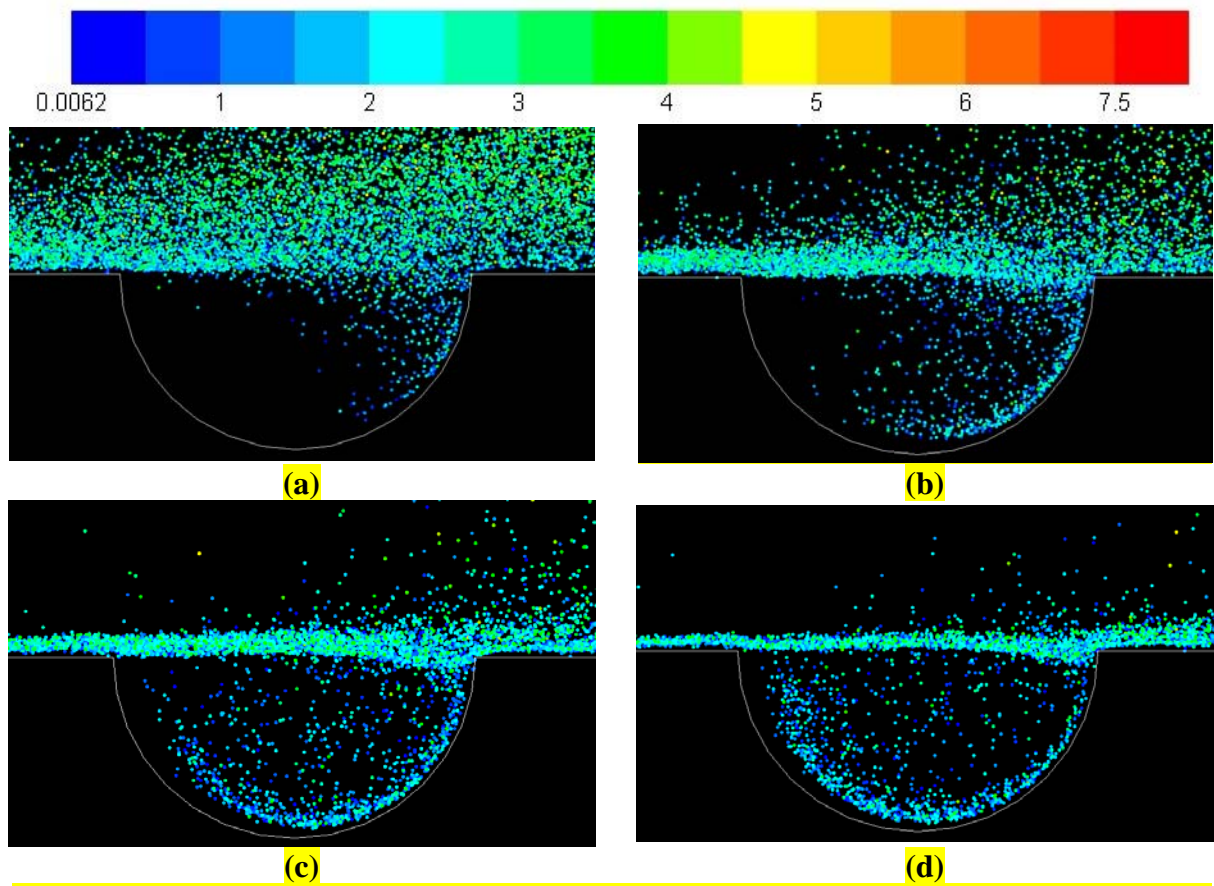


**Figure 10. Deposition location for 0.5  $\mu\text{m}$  particles at the timestep of (a) 0.006 s (b) 0.008 s (c) 0.01 s (d) 0.012 s**

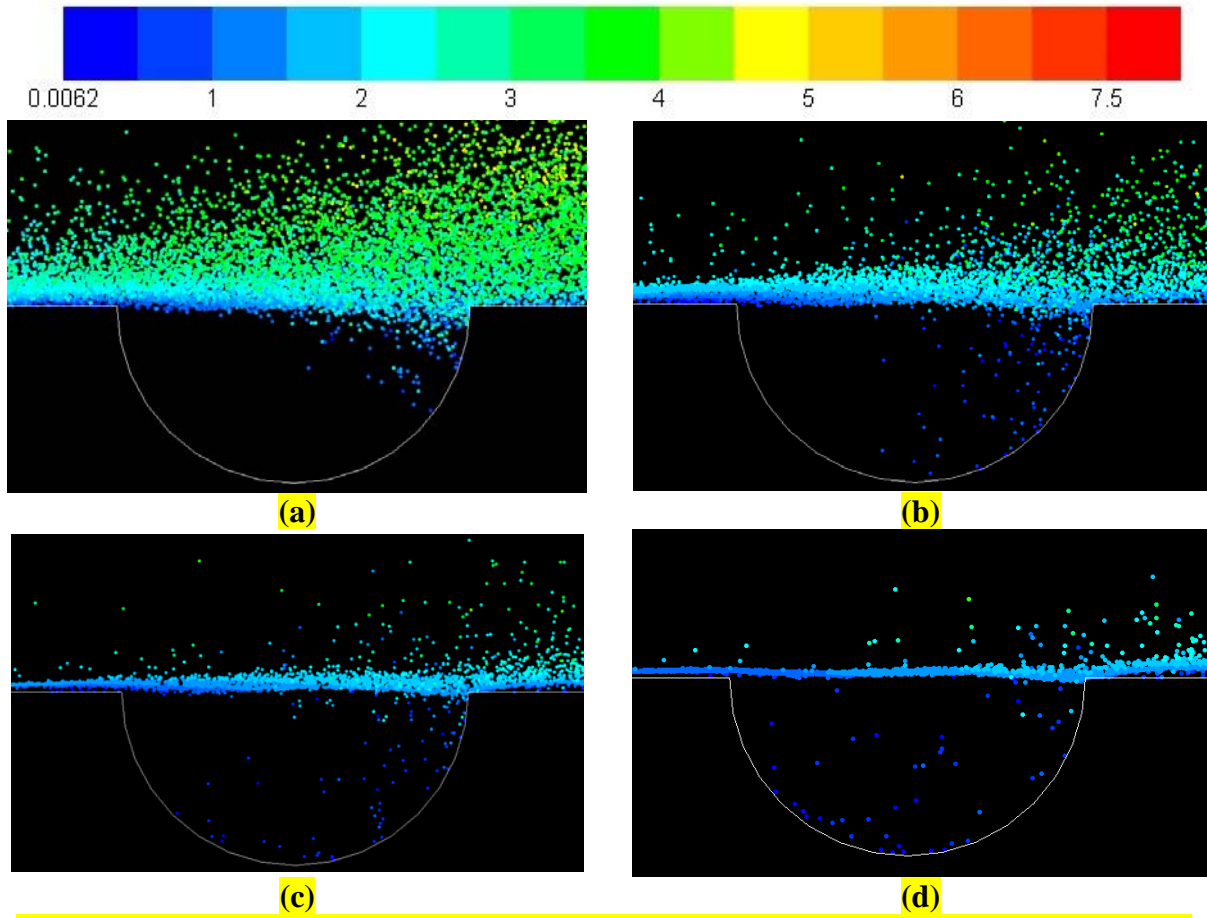


**Figure 11. Deposition location for 2.5  $\mu\text{m}$  particles at time step of (a) 0.006 s (b) 0.008 s (c) 0.01 s (d) 0.012 s**

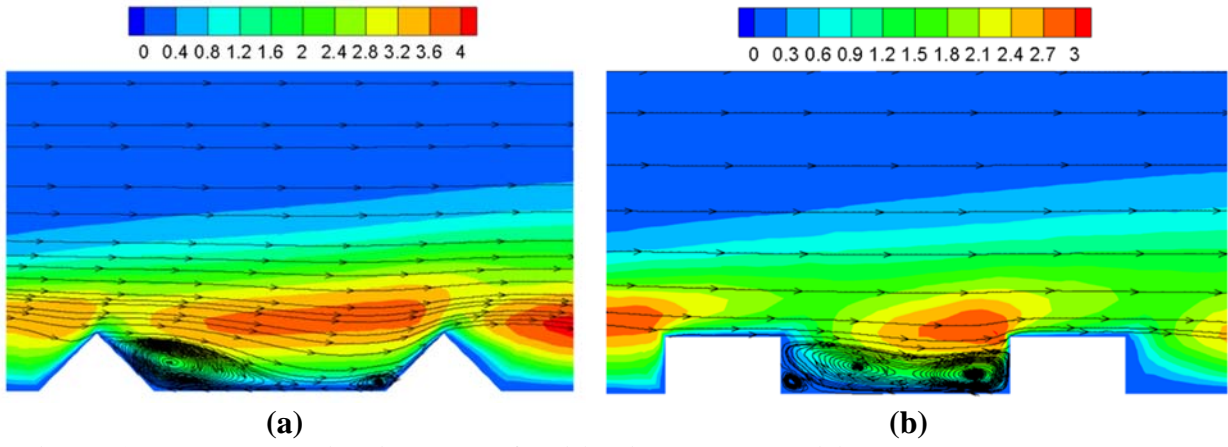


**Figure 12. Turbulent kinetic energy for (a) triangular and (b) rectangular shapes at the p/e of 6**

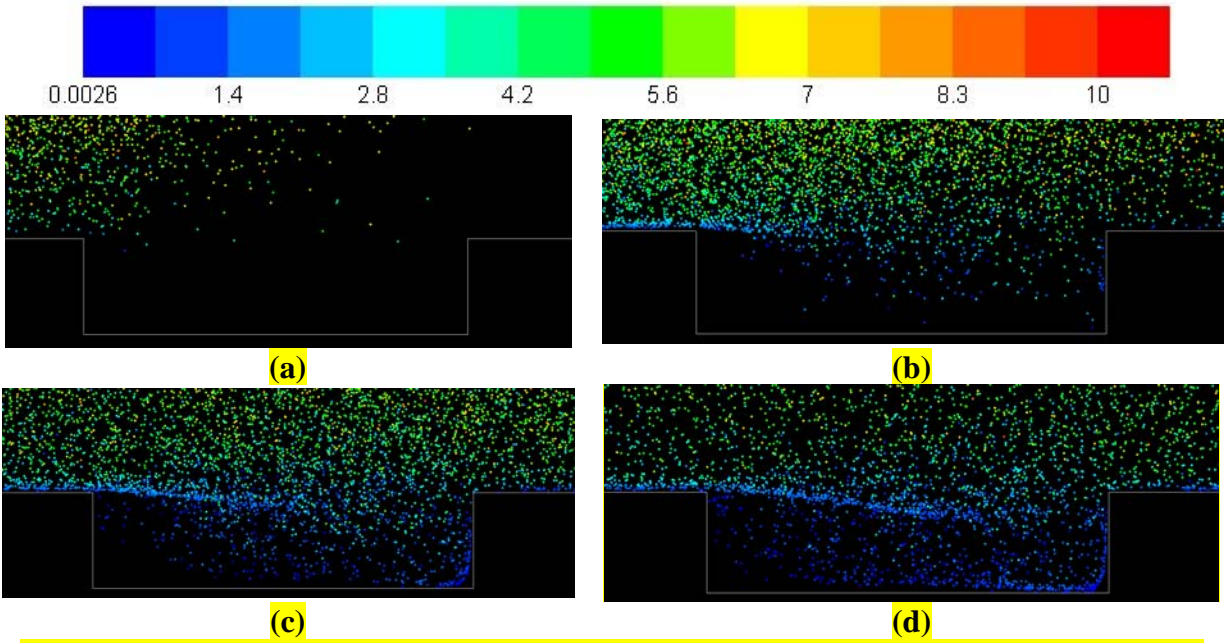


**Figure 13. Lagrangian particle tracking results on the rectangular patterned surface at the time step of (a) 0.007 s (b) 0.009 s (c) 0.011 s and (d) 0.013 s**

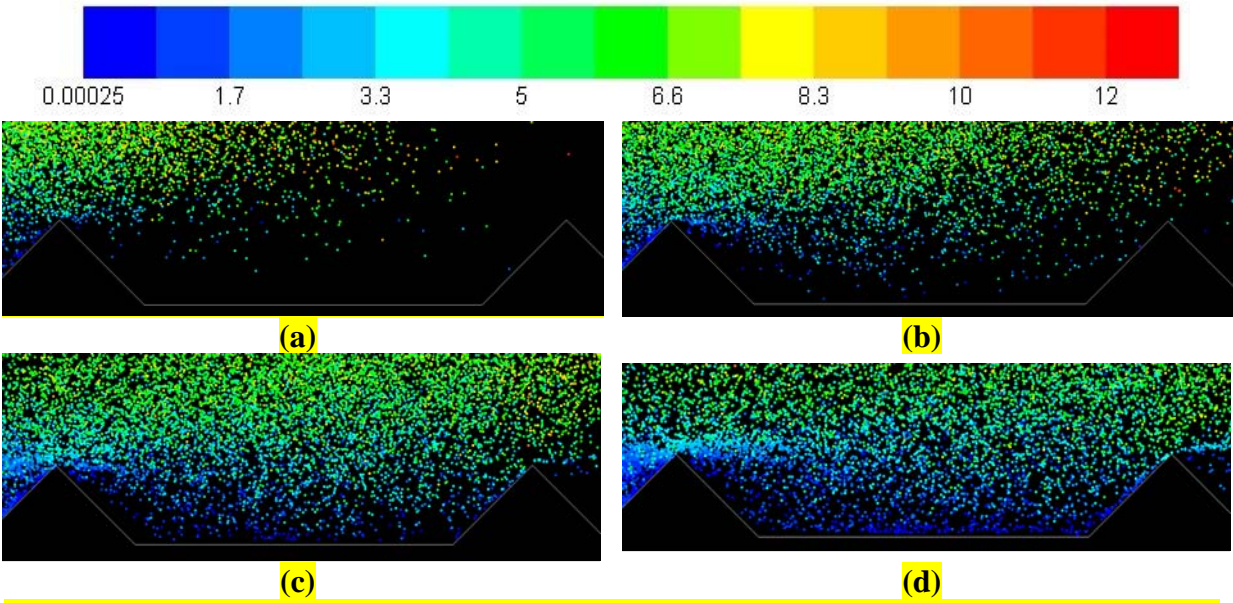


**Figure 14. Lagrangian particle tracking results on the triangular patterned surface at the time step of (a) 0.005 s (b) 0.006 s (c) 0.007 s and (d) 0.008 s**